

Article

Impact Toughness Dependent on Annealing Temperatures in 0.16C-6.5Mn Forged Steel for Flywheel Rotors

Tinghui Man *, Jun Wang, Hongshan Zhao *  and Han Dong

School of Materials Science and Engineering, Shanghai University, Shanghai 200444, China; wj1415477560@shu.edu.cn (J.W.); 13910077790@163.com (H.D.)

* Correspondence: mantinghuilove@163.com (T.M.); boyushankf@126.com (H.Z.)

Abstract: For the application of forged medium-Mn steels on flywheel rotors, the effect of annealing temperatures from 300 °C to 650 °C on the impact toughness of 0.16C-6.5Mn forged steel was investigated to demonstrate the microstructural characteristics and austenite reverse transformation determining the impact toughness. The results obtained through standard Charpy V-notch impact tests at ambient temperature show that the impact absorbed energy holds at lower than 10 J almost constantly at annealing temperatures of 300 °C to 500 °C, and a representative intergranular fracture is presented. At an annealing temperature of 600 °C, the impact absorbed energy increases to 147 J, with the ductile fracture characteristics showing plenty of fine dimples, and the high impact toughness is attributed to the high volume fraction above 30% and the moderate stability of reverted austenite. Subsequently, the annealing temperature rises higher than 600 °C, the impact absorbed energy decreases, and the fracture morphology shows brittleness characterized by more flat facets of intergranular fractures and small quasi-cleavage facets, presumably corresponding to the insufficient transformation and twinning-induced plasticity effect due to weakening the Mn partitioning from quenched martensite to reverted austenite, which results in lower austenitic stability. Furthermore, the ductile-to-brittle transition temperature (DBTT) of the 0.16C-6.5Mn forged steel annealed at 600 °C, which holds the highest impact absorbed energy, and is explored for the possibility of flywheel rotor application in a service environment. The DBTT reaches −21 °C, obtained through the Boltzmann function, and the impact absorbed energy is approximately 72 J.



Citation: Man, T.; Wang, J.; Zhao, H.; Dong, H. Impact Toughness Dependent on Annealing Temperatures in 0.16C-6.5Mn Forged Steel for Flywheel Rotors. *Metals* **2024**, *14*, 501. <https://doi.org/10.3390/met14050501>

Academic Editors: Koh-ichi Sugimoto and Tomohiko Hojo

Received: 28 March 2024

Revised: 21 April 2024

Accepted: 21 April 2024

Published: 25 April 2024



Copyright: © 2024 by the authors. Licensee MDPI, Basel, Switzerland. This article is an open access article distributed under the terms and conditions of the Creative Commons Attribution (CC BY) license (<https://creativecommons.org/licenses/by/4.0/>).

Keywords: flywheel rotors; medium-Mn forged steels; impact toughness; ductile-to-brittle transition temperature; austenite reverse transformation

1. Introduction

With the gradual depletion of global fossil fuels and the deterioration of the ecological environment, the Chinese government has committed to ‘strive to peak carbon dioxide emissions by 2030 and achieve carbon neutrality by 2060’ to deal with these problems [1]. Renewable energy sources have been created as an ideal and feasible method to resolve the shortage of energy, but their intermittent nature inhibits their application; thus, the development of energy storage systems plays a role in providing high-quality and sustainable clean energy [2,3]. Flywheel energy storage systems have attracted greater interest in industrial applications that utilize the intertransmission of electrical and mechanical energy [3–6]. For flywheel rotors, their materials and structures are extremely important, especially the materials. Usually, composites and metals are used to manufacture flywheel rotors [7–11]. Among them, composite materials hold low density and metals of excellent tensile strength to reach ultra-high speed, which can acquire high energy storage density for the purpose of a continuous energy supply [7–9]. Although the metal materials of 40, 40Cr and 42CrMo are typically used for flywheel rotors, which are old and less efficient due to high density, low yield strength and poor hardenability, they exhibit considerable advantages such as cost-effectiveness and easy manufacturing [7,10,11].

Medium-Mn steels, as a primary representative of advanced high-strength steels in the application of automotive light weight, have received widespread attention owing to their outstanding strength and ductility through regulating the microstructure in multiphase, metastable and multiscale aspects during austenite reverse transformation annealing [12–16]. It is well known that the Mn element is an austenitic stabilizing element that expands the austenitic phase zone and significantly improves hardenability, which is of great benefit in manufacturing the large forging of flywheel rotors [17]. Moreover, medium-Mn steels possess outstanding specific strength among the metal materials and a low production cost. Based on these advantages, medium-Mn steels are an ideal choice to become competitive and gain attention in flywheel rotors.

As mentioned above, many studies focused on the tensile properties of medium-Mn steels after being hot-rolled and/or cold-rolled as well as with austenite reverse transformation annealing. The materials' toughness is also of importance for flywheel rotors under high-speed rotation. Thus, a thorough understanding of the impact toughness at various annealing temperatures is essential for the design of medium-Mn steels in the application of flywheel rotors. In addition, the service environment of flywheel rotors needs to consider low-temperature conditions. The ductile-to-brittle transition temperature (DBTT), which is a significant parameter for evaluating the materials' transition from ductility to brittleness to predict the low-temperature toughness, must be investigated thoroughly. Some studies on impact toughness and DBTT in correlation to austenite reverse transformation in medium-Mn steels have been conducted [17–24]. Sun et al. [17] investigated the effect of an intercritical tempering temperature on the impact toughness of an Fe-0.05C-5.42Mn medium-Mn steel, which included a process of melting, forging and hot-rolling, and they found that the impact toughness was enhanced for intercritical tempering at 625 °C and 665 °C compared to traditional tempering at 570 °C. In this case, the reversed austenite enriched with C and Mn formed between martensite laths was the reason for the increased absorbed crack propagation energy, and the stability of reversed austenite played a role in the DBTT of the Fe-0.05C-5.42Mn medium-Mn steel. Dutta et al. [18] reported the enhancement of tensile properties and impact toughness in an Fe-0.06C-12Mn-3Al medium-Mn steel produced by melting, hot-rolling and cold-rolling processes, suggesting that the austenitization treatments at 850 °C revealed higher toughness than those at 1100 °C, owing to the existence of smaller colonies of reversed austenite. The smaller colonies of reversed austenite brought a more homogeneous microstrain distribution and resulted in a more global transformation and twinning-induced plasticity behaviors, which improved the impact toughness. Han et al. [19] published a study on the impact toughness of an Fe-0.1C-7Mn medium-Mn steel under hot-rolling or cold-rolling processes. The higher DBTT and low-temperature impact toughness contributed to the lath-shaped morphology of the hot-rolled sample compared to the globular-shaped morphology of the cold-rolled sample, which is due to intergranular cracking along the austenite grain boundaries decorated by C and Mn in the hot-rolled sample. Hu et al. [23] studied the combined mechanical properties of a hot-rolled Fe-0.045C-5.6Mn medium-Mn steel and revealed that the thermal and mechanical stability of austenite decreased with an increasing annealing temperature. The crack initiation energy and crack propagation energy were increased via dynamic stress partitioning and relaxation together with the transformation of metastable austenite, corresponding to moderate austenite stability. The production processes used in the above-mentioned literature were melting, forging, hot-rolling and/or cold-rolling, followed by various heat treatments for medium-Mn steels; however, research on the impact toughness of medium-Mn forged steels, especially for low ambient temperatures, is scarce. Therefore, this work aims to make clear the impact toughness dependent on the annealing temperatures and obtain the DBTT in a 0.16C-6.5Mn forged steel. Moreover, the microstructural evolution and Mn partitioning of the 0.16C-6.5Mn steel during the whole process of forging to austenite reverse transformation annealing are discussed.

2. Experimental Method

A 3000 kg ingot of the experimental medium-Mn forged steel was smelted using a high-frequency vacuum induction furnace and electroslag remelting, and the chemical composition is Fe-0.16C-6.5Mn-0.15Si-0.008P-0.001S-0.015Cr-0.02Mo-0.03Ni-0.02Al-0.0045Co-0.017Cu-0.0008Nb-0.0017Ti-0.0032V-0.0005O-0.004N in wt.% in this work, hereafter noted as 0.16C-6.5Mn. The ingot was homogenized at 1200 °C, then forged between 1150 °C and 850 °C into a disk with dimensions of $\Phi 800 \text{ mm} \times 400 \text{ mm}$, followed by annealing to 550 °C for 8 h, and finally cooled to ambient temperature (around 20 °C) in air. The samples for the standard Charpy V-notch impact tests were cut from the forged bars to dimensions of 10 mm \times 10 mm \times 55 mm according to the standard GB/T 229-2020 [25]. Then, the samples were heated at 880 °C for 0.5 h and air-cooled to ambient temperature, followed by austenitizing at 850 °C for 1 h and water-quenching to form martensite in the 0.16C-6.5Mn steel. Subsequently, the samples were, respectively, annealed at 300 °C to 650 °C for 4 h and then cooled to ambient temperature in air. The heat treatment process of the 0.16C-6.5Mn forged steel is shown in Figure 1.

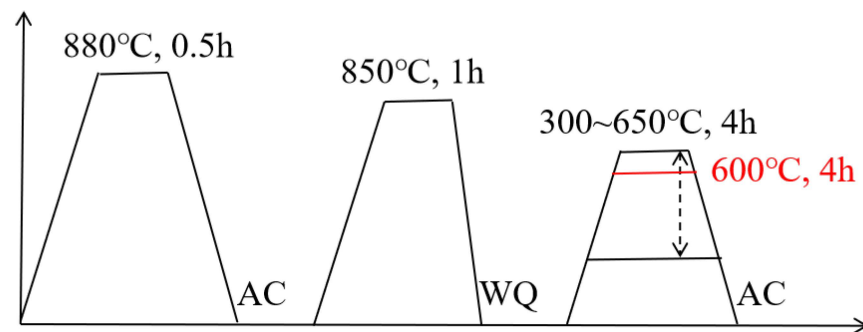


Figure 1. The heat treatment process of the 0.16C-6.5Mn forged steel.

A set of the samples was subjected to annealing temperatures from 300 °C to 650 °C through standard Charpy V-notch impact tests using a SUNS impact tester with a capacity of 450 J at ambient temperature to study the relationship between the impact toughness and annealing temperature. Another set of samples subjected to an annealing temperature of 600 °C (corresponding the to red line in Figure 1) was tested at various temperatures (−196 °C, −150 °C, −100 °C, −78 °C, −60 °C, −40 °C, −20 °C, 0 °C, 20 °C, 50 °C, 80 °C) to demonstrate the DBTT of the 0.16C-6.5Mn forged steel. Impact test temperatures below ambient temperature were achieved by cooling into an alcoholic solution with dry ice and liquid nitrogen, respectively, for more than 20 min; the impact tests were completed within 5 s, and the temperatures were monitored with an attached thermometer through the impact test cryogenic instrument NCS-LTI-196. For the impact test temperatures above ambient temperature, the samples were heated for 5 min in a furnace, and the impact tests were finished in 20 s. For each condition, three samples were tested, and their average value was used as the final datapoint in this work. The fractured surfaces of impact test samples were observed via a Bright MAS 600 optical microscope (OM) and ZEISS Sigma 300 field emission scanning electron microscope (SEM) after ultrasonic cleaning in an acetone solution for several minutes. The samples with dimensions of 10 mm \times 10 mm \times 10 mm were cut from the impact test samples for microstructural observations using SEM, Rigaku SmartLab X-ray diffraction (XRD) and Oxford electron backscattered diffraction (EBSD). Post-test, the samples underwent polishing and etching with an 8 vol.% nitric acid–alcohol solution, prepared for SEM and XRD assessments. The XRD measurements were carried out using Cu K α radiation with a scanning rate of 2°/min. The obtained XRD results were post-processed using MDI Jade 6 software, and the integrated intensities of the

(200) γ , (220) γ , (311) γ , (200) α and (211) α diffraction peaks were calculated to quantitatively measure the volume fraction of austenite with the modified Miller method [24].

$$V_{\gamma} = \frac{1.4I_{\gamma}}{I_{\alpha} + 1.4I_{\gamma}} \quad (1)$$

where I_{γ} and I_{α} are the integrated intensities of the austenite and ferrite/martensite diffraction peaks, respectively.

The samples for EBSD measurements were mechanically ground and electrolytically polished using a solution composed of 8 vol.% perchloric acid, 73 vol.% ethyl alcohol, 10 vol.% butyl cellosolve and 9 vol.% distilled water, under a voltage of 45 V. The EBSD measurements were operated at an accelerating voltage of 20 kV with a tilt angle of 70°, using a scanning step size of 0.1 μm , and the obtained EBSD results were post-processed using AZtecCrystal software 5.

3. Results and Discussion

3.1. Impact Toughness

Figure 2 shows the Charpy V-notch impact absorbed energy dependent on annealing temperatures of 300 °C to 650 °C in the 0.16C-6.5Mn forged steel, which is obtained at ambient temperature. It is found that the impact absorbed energy remains almost constantly lower than 10 J at annealing temperatures from 300 °C to 500 °C, then suddenly increases to 147 J at 600 °C, whereafter it decreases down to 41 J. The sample annealed at 600 °C holds the best impact absorbed energy, which is related to the volume fraction and stability of reverted austenite obtained via austenite reverse transformation annealing. Generally, the total impact energy is composed of three stages: crack initiation, crack stable propagation and crack unstable propagation. The crack initiation corresponds to the difficulty of crack formation, which has a relationship with plastic deformation. Therefore, this suggests that a more sustainable transformation and twinning-induced plasticity effect may occur during impact processing for the 0.16C-6.5Mn forged steel subjected to an annealing temperature of 600 °C.

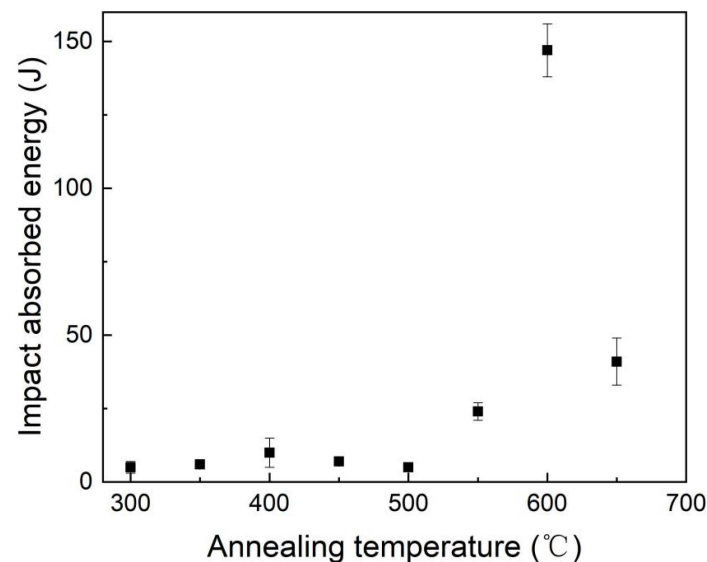


Figure 2. Charpy V-notch impact absorbed energy versus annealing temperature curve for the 0.16C-6.5Mn forged steel.

Figure 3 shows OM images of the impact fracture of the 0.16C-6.5Mn forged steel subjected to various annealing temperatures from 300 °C to 650 °C. Furthermore, high-magnification images of the impact fracture at 350 °C, 450 °C, 600 °C and 650 °C are shown in Figure 4, which are characterized by SEM. In general, the fracture surface should

be divided into three zones: the fibrous zone, the shear lip zone and the radial zone. From Figure 3a–f, the fracture surfaces are typical of a brittle fracture, indicating relative flatness and mainly consisting of a radial zone with rough tearing ridges at an annealing temperature lower than 550 °C. Another typical characteristic of brittle fractures is the intergranular fracture shown in Figure 4a,b. The prevalent intergranular fracture with few quasi-cleavage features and fine dimples exists, and the detached boundaries of intergranularly fractured grains show both rugged facets and flat facets. This implies an intergranular fracture along the boundaries of prior austenite grains for an annealing temperature lower than 550 °C. In contrast, at an annealing temperature of 600 °C, the fracture surface exhibits three zones (fibrous, shear lip and radial) in Figure 3g, especially featuring a clear fibrous zone. It can be seen that there is a great number of shallow dimples in Figure 4c, considered a ductile fracture mode, which suggests that a large plastic deformation occurred, leading to the stress release at the main crack tips. In addition, the different sizes of shallow dimples can absorb more impact energy. In Figures 3h and 4d, a mixed fracture mode containing brittle and ductile fracture features is seen, characterized by more flat facets of intergranular fractures and small quasi-cleavage facets. Based on the impact tests and post-mortem, the prior austenite grain boundaries should be the weakest feature in the microstructure of the 0.16C-6.5Mn forged steel. The change in the fracture mode from the brittle fracture to the ductile fracture, then to the mixed fracture at various annealing temperatures, should be immediately correlated to the microstructural evolution in the 0.16C-6.5Mn forged steel.

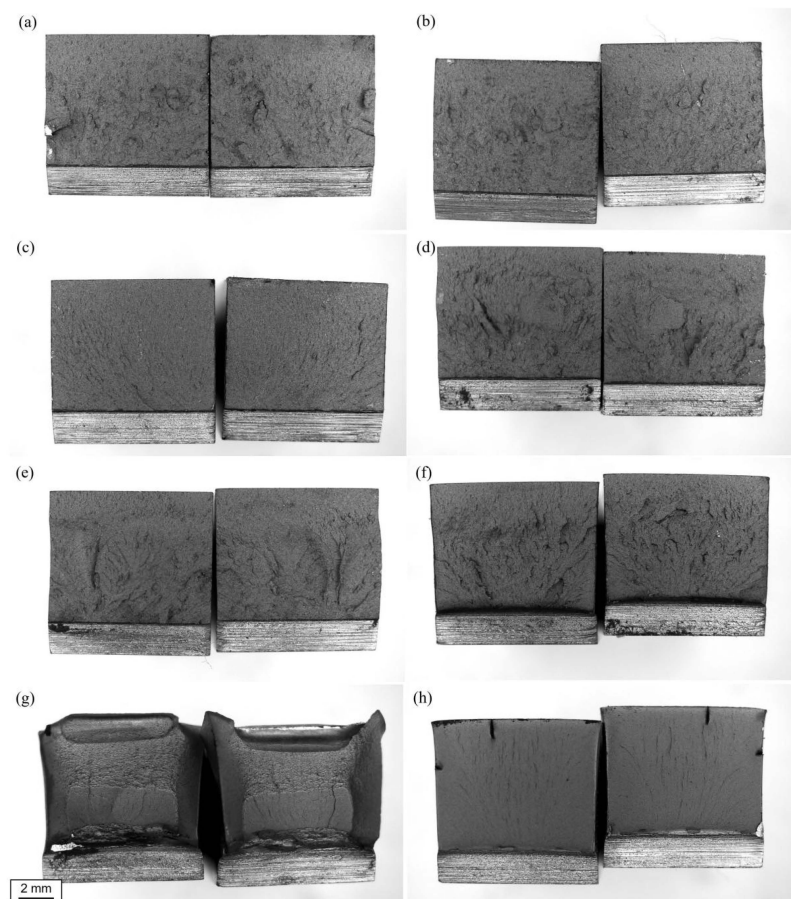


Figure 3. OM images of the impact fracture of the 0.16C-6.5Mn forged steel subjected to various annealing temperatures of (a) 300 °C, (b) 350 °C, (c) 400 °C, (d) 450 °C, (e) 500 °C, (f) 550 °C, (g) 600 °C and (h) 650 °C.

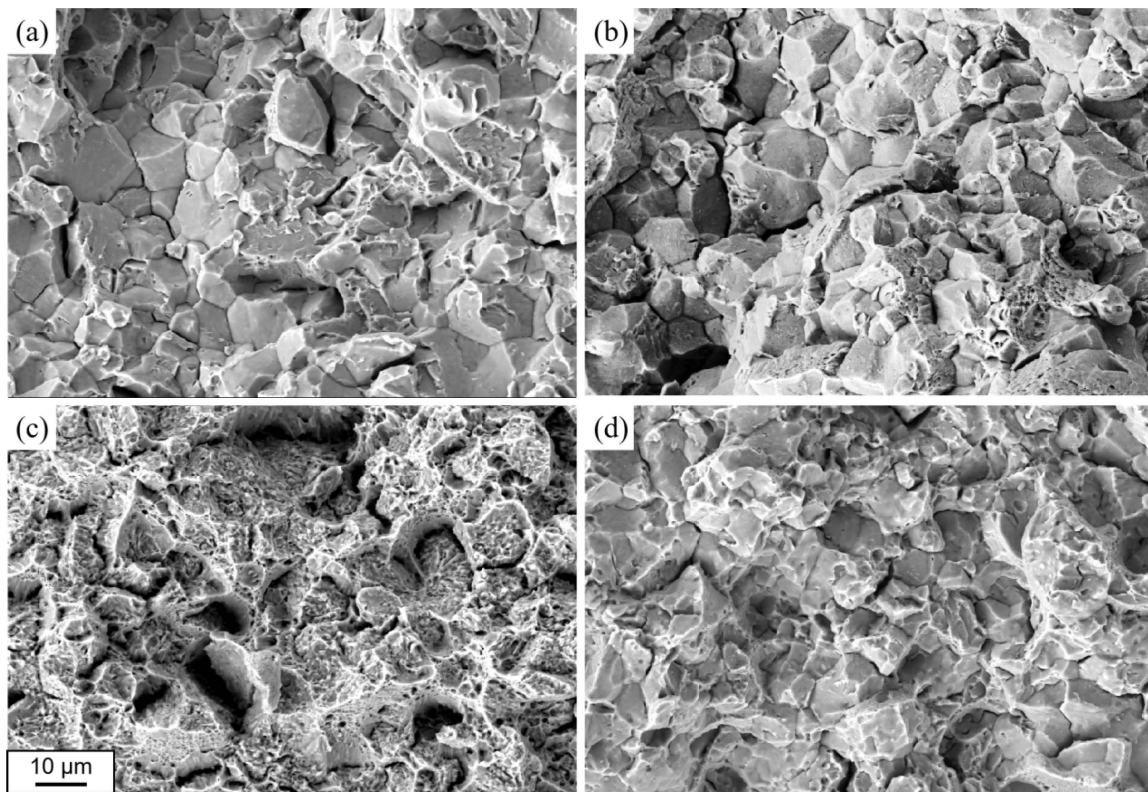


Figure 4. SEM images of the impact fracture of the 0.16C-6.5Mn forged steel subjected to annealing temperatures of (a) 350 °C, (b) 450 °C, (c) 600 °C and (d) 650 °C.

3.2. Microstructural Evolution

The microstructures of the 0.16C-6.5Mn forged steel subjected to annealing temperatures from 300 °C to 650 °C were detected using SEM and XRD measurements, which are displayed in Figures 5 and 6a, respectively. Figure 6b shows the volume fraction of austenite calculated with Equation (1) using the Miller method. Figure 7 shows phase images of the microstructure in the 0.16C-6.5Mn forged steel subjected to annealing temperatures at (a) 400 °C and (b) 600 °C, obtained with EBSD measurements, where the red and green in the phase images correspond to bcc and fcc structures. It can be seen from Figure 5a–d that the microstructures in the samples annealed at 300 °C to 500 °C are composed of ferrite, martensite and cementite. Also, the microstructure clearly shows the prior austenite grain boundaries at 300 °C to 500 °C. However, the remaining austenite is difficult to identify accurately via SEM observation. Thus, combined with XRD spectra, it is found that the samples for annealing temperatures of 300 °C to 500 °C do not present any austenite diffraction peaks of (111) γ , (200) γ , (220) γ or (311) γ . Meanwhile, an almost-bcc structure is presented in the microstructure at an annealing temperature of 400 °C, as shown in Figure 7a, and it has a proportion above 95%, suggesting that very little austenite was formed. When the annealing temperature was increased to 550 °C, the cementite gradually began to dissolve, and the prior austenite grain boundaries disappeared, with some remaining interstices in Figure 5f; at this point, there were no diffraction peaks of austenite. At this moment, the lower impact toughness with a brittle fracture is believed to be from the segregation of Mn and C during annealing processing because Mn and C can embrittle the prior austenite grain boundaries [26,27]. There is less P segregation in the 0.16C-6.5Mn forged steel, which is a reason for embrittling grain boundaries [22,28]. Furthermore, the morphology of the 600 °C and 650 °C samples shows a lath-shaped microstructure in Figure 5g,h. The XRD profile shows all the diffraction peaks of the (111) γ , (200) γ , (220) γ and (311) γ for the samples annealed at 600 °C and 650 °C in Figure 6. Additionally, the fcc structure in the microstructure of the 600 °C annealed sample is clearly displayed in

green in Figure 7b, which indicates the occurrence of austenite. All the results related to the microstructure indicate that the austenite reverse transformation occurs during annealing treatments, and the reverted austenite precipitates at the locations of the forged and quenched martensite showing a lath shape. Moreover, the strength of the diffraction peaks of $(111)\gamma$, $(200)\gamma$, $(220)\gamma$ and $(311)\gamma$ decreases with an increase in annealing temperature from 600 °C to 650 °C. In Figure 6b, the calculated volume fraction of austenite in the 600 °C and 650 °C samples is 31.1% and 16.3%, respectively. And, the volume fraction of austenite is approximately 30% for an annealing temperature of 600 °C, which is an average value obtained based on the three different detected areas using EBSD analysis. The volume fraction of austenite measured using EBSD is in accordance with that obtained via XRD. It is known that the formation of reversed austenite is accompanied by the diffusion of the substitutional atoms Mn and interstitial atoms C during the annealing process [26,29–31]. The atoms Mn and C diffuse from the interior of martensite plates to the interface, and thin reversed austenite films nucleate and grow mainly along the lath or block boundaries. The lath-shaped reversed austenite forms rather than the globular shape at 600 °C due to the absence of recrystallization of the forged and quenched martensite, indicating that the initial martensite characteristics, such as prior austenite grain boundary, packet, block and lath, have a significant effect on the morphology of reversed austenite. The morphology of some reversed austenite changes from the film type to the block type when the annealing temperature is increased to 650 °C. The Mn and C contents in austenite decrease to different degrees when the annealing temperature is increased, and this phenomenon agrees with the expected partitioning of Mn and C into reversed austenite. Since both Mn and C decrease the martensite transformation start temperature, the thermal stability of reversed austenite is lowered [23]. The thermal stability of austenite is also affected by the grain size [32]. Thus, the majority of reversed austenite subjected to an annealing temperature of 600 °C was thermally stable during cooling processing to ambient temperature compared to that at 650 °C, which is attributed to the reduced Mn and C enrichment and coarse grain size. As a result, a small volume fraction of reverted austenite is not capable of releasing the strain concentration of deformation-induced martensite during impact processing. In addition, the segregation of Mn at the grain boundaries and the decohesion further deteriorate the impact toughness, resulting in intergranular fractures at 650 °C. It is presumed that the main factor leading to a significant reduction in the impact toughness from 147 J to 41 J at an annealing temperature of 600 °C increased to 650 °C is the reverted austenite. The presence of the reverted austenite improves the impact toughness and is attributed to a crack deflecting or blunting, which reduces crack propagation through local martensite transformation during impact processing. That is to say, the highest impact absorbed energy for the 600 °C sample is believed to be related to the volume fraction and stability of reverted austenite, which suggests that the high volume fraction and stability of reverted austenite will guarantee the sustainability of the transformation and twinning-induced plasticity effect to suppress crack propagation during the impact process to gain exceptional toughness in flywheel rotor applications.

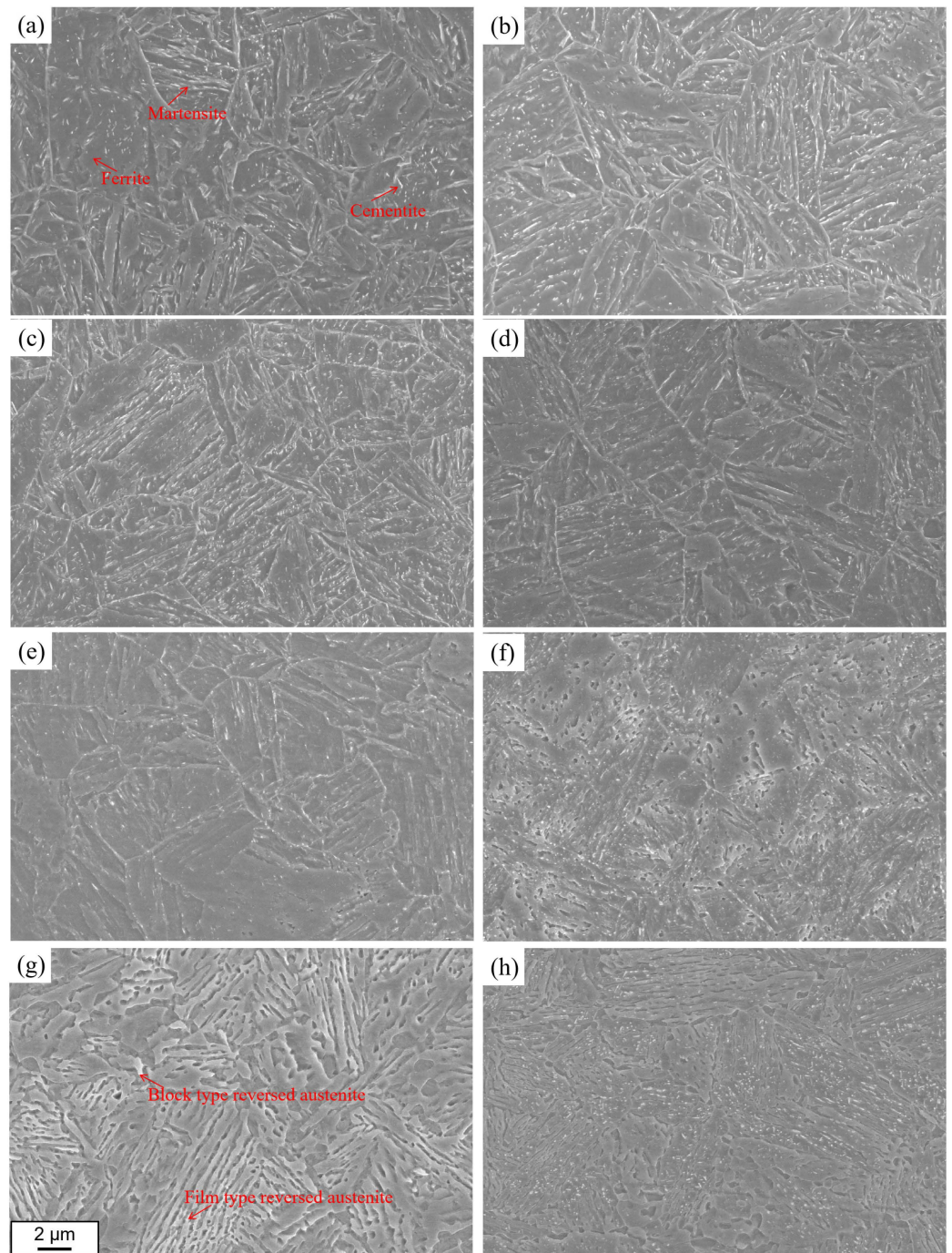


Figure 5. SEM images of the microstructure of the 0.16C-6.5Mn forged steel subjected to various annealing temperatures: (a) 300 °C, (b) 350 °C, (c) 400 °C, (d) 450 °C, (e) 500 °C, (f) 550 °C, (g) 600 °C and (h) 650 °C.

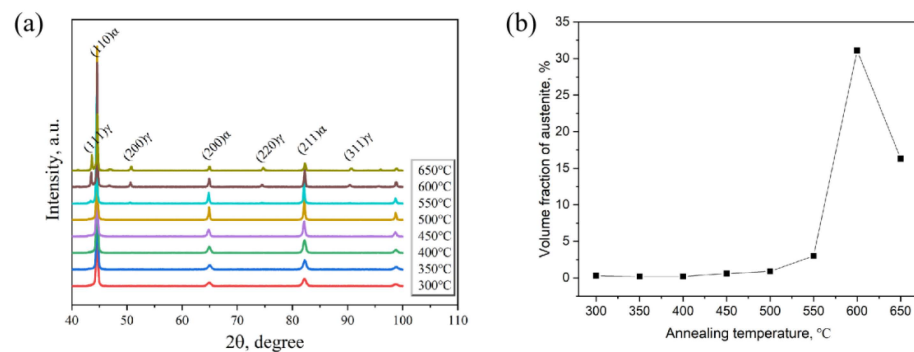


Figure 6. (a) XRD spectra and (b) the volume fraction of austenite in the 0.16C-6.5Mn forged steel subjected to annealing temperatures from 300 °C to 650 °C.

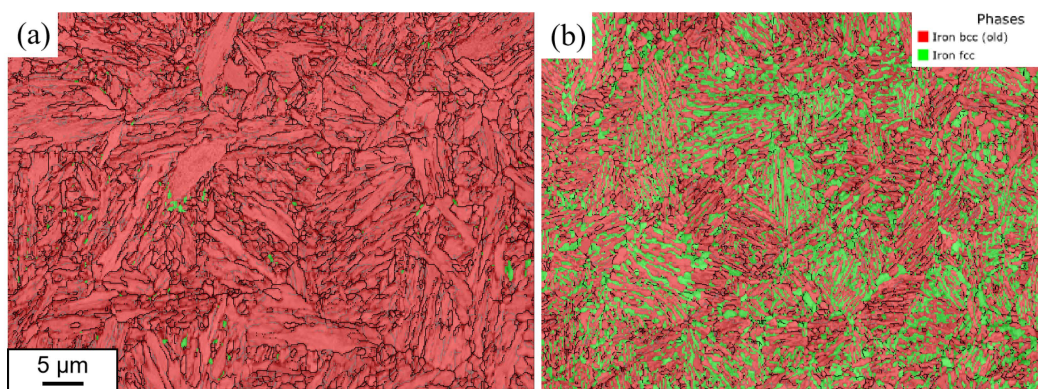


Figure 7. Phase images of the microstructure of the 0.16C-6.5Mn forged steel subjected to annealing temperatures of (a) 400 °C and (b) 600 °C.

3.3. Ductile-to-Brittle Transition Temperature

Many studies have suggested that the Boltzmann function is reasonably used to fit the impact energy of components at different temperatures, which has a better correlation coefficient and smaller residual error in various mathematical models used in the fitting analysis for evaluating the DBTT [33–36]. The Boltzmann function is as shown in Equation (2):

$$A_{KV} = \frac{A_1 - A_2}{1 + \exp((T - x_0)/\Delta x)} + A_2 \quad (2)$$

Here, A_{KV} represents the impact energy with a unit of J, T is the test temperature with a unit of °C, x_0 is the DBTT with a unit of °C, Δx is the temperature range of the DBTT zone with a unit of °C, A_1 is the lower-bound energy with a unit of J and A_2 is the upper-bound energy with a unit of J.

The samples subjected to an annealing temperature of 600 °C for 4 h underwent Charpy V-notch impact tests at various test temperatures from −196 °C to 80 °C. In this work, the Boltzmann function is used to be the function of DBTT, and the arithmetic mean value of the maximum impact work (upper shelf energy) and the minimum impact energy (lower shelf energy) is defined as the DBTT. Figure 8 shows the Charpy V-notch impact absorbed energy versus a test temperature curve of the 0.16C-6.5Mn forged steel subjected to an annealing temperature of 600 °C. In the curve, the impact absorbed energy is almost completely maintained in a range of 80 °C to 20 °C and then drops with decreasing test temperatures from 0 °C to −100 °C, and it holds a similar value in a range of −100 °C to −196 °C. Moreover, the DBTT of the steel subjected to annealing at 600 °C is −21 °C, obtained via Equation (1), and the impact absorbed energy is approximately 72 J.

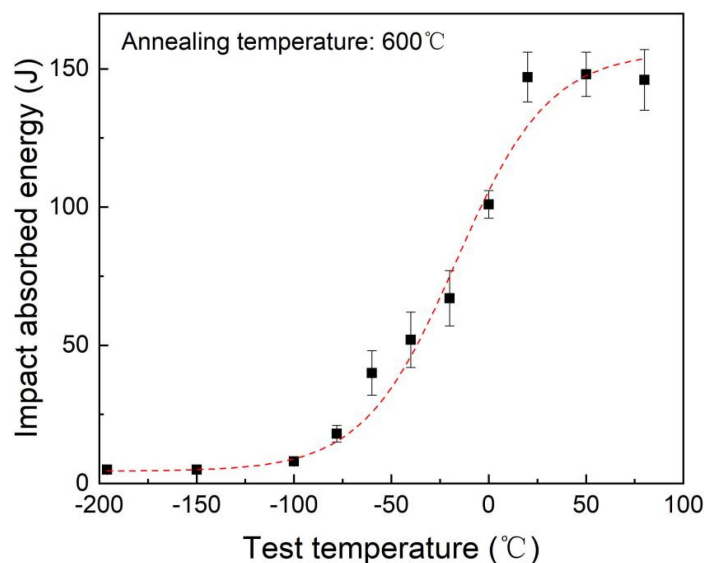


Figure 8. Charpy V-notch impact absorbed energy versus test temperature curve for the 0.16C-6.5Mn forged steel subjected to an annealing temperature of 600 °C.

4. Conclusions

The effect of annealing temperature on impact toughness and the DBTT for 0.16C-6.5Mn forged steel was investigated to provide a reference frame for austenite reverse transformation processibility for a medium-Mn forged steel. The 0.16C-6.5Mn forged steel exhibited a high impact absorbed energy of 147 J at an annealing temperature of 600 °C, with the volume fraction of reverted austenite reaching above 30% with moderate stability, which suggests that the more sustainable transformation and twinning-induced plasticity effect took place and could suppress crack propagation to improve impact toughness. Upon increasing the annealing temperature to 650 °C, the impact absorbed energy decreased to 41 J, and the fractured morphology was characterized by a brittle feature that revealed more flat facets of intergranular fractures and small quasi-cleavage facets. Furthermore, the DBTT of the 0.16C-6.5Mn forged steel annealed at an annealing temperature of 600 °C was −21 °C, and the impact absorbed energy was approximately 72 J; this provides a basic foundation for the toughness of medium-Mn forged steels for use in the field of flywheel rotors.

Author Contributions: Conceptualization, T.M. and H.Z.; Methodology, T.M. and H.Z.; Formal analysis, T.M. and J.W.; Investigation, T.M. and J.W.; Resources, T.M. and H.D.; Data curation, T.M. and H.D.; Writing—original draft, T.M.; Writing—review & editing, T.M. and H.Z.; Supervision, T.M. and H.Z.; Project administration, H.Z. and H.D.; Funding acquisition, T.M. All authors have read and agreed to the published version of the manuscript.

Funding: The authors were sponsored by the Natural Science Foundation of Shanghai with grant number 23ZR1421700.

Data Availability Statement: The raw data supporting the conclusions of this article will be made available by the authors on request.

Conflicts of Interest: The authors declare no conflicts of interest.

References

1. Report of the Chinese Government in 2021. Available online: http://www.qsttheory.cn/yaowen/2022-03/12/c_1128465058.htm (accessed on 12 March 2022).
2. Pei, Y.; Andrea, C.; Silvio, V.; Chai, F.; Alberto, T. Flywheel energy storage systems for power systems application. In Proceedings of the 6th International Conference on Clean Electrical Power (ICCEP), Santa Margherita Ligure, Italy, 27–29 June 2017.
3. Abdalla, A.N.; Nazir, M.S.; Tao, H.; Cao, S.; Ji, R.; Jiang, M.; Yao, L. Integration of energy storage system and renewable energy sources based on artificial intelligence: An overview. *J. Energy Storage* **2021**, *40*, 102811. [[CrossRef](#)]

4. Pullen, K.R. The Status and Future of Flywheel Energy Storage. *Joule* **2019**, *3*, 1394–1399. [[CrossRef](#)]
5. Li, X.; Palazzolo, A. A review of flywheel energy storage systems: State of the art and opportunities. *J. Energy Storage* **2021**, *46*, 103576. [[CrossRef](#)]
6. Nguyen, X.P.; Hoang, A.T. The Flywheel Energy Storage System: An Effective Solution to Accumulate Renewable Energy. In Proceedings of the 2020 6th International Conference on Advanced Computing and Communication Systems (ICACCS), Coimbatore, India, 6–7 March 2020.
7. Kale, V.; Aage, N.; Secanell, M. Augmented Lagrangian approach for multi-objective topology optimization of energy storage flywheels with local stress constraints. *Struct. Multidiscip. Optim.* **2023**, *66*, 231. [[CrossRef](#)]
8. Arnold, S.; Saleeb, A.; Al-Zoubi, N. Deformation and life analysis of composite flywheel disk systems. *Compos. Part B Eng.* **2002**, *33*, 433–459. [[CrossRef](#)]
9. Mittelstedt, M.; Hansen, C.; Mertiny, P. Design and Multi-Objective Optimization of Fiber-Reinforced Polymer Composite Flywheel Rotors. *Appl. Sci.* **2018**, *8*, 1256. [[CrossRef](#)]
10. Genta, G. *Kinetic Energy Storage*; Elsevier BV: Amsterdam, The Netherlands, 1985.
11. Wu, X.; Chen, Y.; Liu, Y. Structure optimization of metal rotor of grid-connected flywheel energy storage system. *Acta Energ. Solaris Sinica* **2021**, *42*, 317.
12. Cao, W.Q.; Wang, C.; Shi, J.; Wang, M.Q.; Hui, W.J.; Dong, H. Microstructure and mechanical properties of Fe-0.2C-5Mn steel processed by ART-annealing. *Mater. Sci. Eng. A* **2011**, *528*, 6661. [[CrossRef](#)]
13. Hu, J.; Li, X.; Meng, Q.; Wang, L.; Li, Y.; Xu, W. Tailoring retained austenite and mechanical property improvement in Al-Si-V containing medium Mn steel via direct intercritical rolling. *Mater. Sci. Eng. A* **2022**, *855*, 143904. [[CrossRef](#)]
14. Lee, S.; De Cooman, B.C. On the selection of the optimal intercritical annealing temperature for medium Mn TRIP steel. *Metall. Mater. Trans. A* **2013**, *44A*, 5018. [[CrossRef](#)]
15. Hu, J.; Du, L.-X.; Sun, G.-S.; Xie, H.; Misra, R. The determining role of reversed austenite in enhancing toughness of a novel ultra-low carbon medium manganese high strength steel. *Scr. Mater.* **2015**, *104*, 87–90. [[CrossRef](#)]
16. Gibbs, P.J.; De Moor, E.; Merwin, M.J.; Clausen, B.; Speer, J.G.; Matlock, D.K. Austenite Stability Effects on Tensile Behavior of Manganese-Enriched-Austenite Transformation-Induced Plasticity Steel. *Met. Mater. Trans. A* **2011**, *42*, 3691–3702. [[CrossRef](#)]
17. Sun, C.; Liu, S.; Misra, R.; Li, Q.; Li, D. Influence of intercritical tempering temperature on impact toughness of a quenched and tempered medium-Mn steel: Intercritical tempering versus traditional tempering. *Mater. Sci. Eng. A* **2018**, *711*, 484–491. [[CrossRef](#)]
18. Dutta, A.; Park, T.M.; Nam, J.-H.; Lee, S.-I.; Hwang, B.; Choi, W.S.; Sandlöbes, S.; Ponge, D.; Han, J. Enhancement of the tensile properties and impact toughness of a medium-Mn steel through the homogeneous microstrain distribution. *Mater. Charact.* **2021**, *174*, 110992. [[CrossRef](#)]
19. Han, J.; da Silva, A.K.; Ponge, D.; Raabe, D.; Lee, S.-M.; Lee, Y.-K.; Hwang, B. The effects of prior austenite grain boundaries and microstructural morphology on the impact toughness of intercritically annealed medium Mn steel. *Acta Mater.* **2016**, *122*, 199–206. [[CrossRef](#)]
20. Man, T.; Jiang, C.; Liu, K.; Liu, T.; Gu, J.; Dong, H. Study on hardenability of large cross-sectional high strength medium-Mn forged steels. *J. Iron Steel Res.* **2022**, *34*, 834.
21. Kim, M.T.; Park, T.M.; Baik, K.-H.; Choi, W.S.; Choi, P.-P.; Han, J. Crucial microstructural feature to determine the impact toughness of intercritically annealed medium-Mn steel with triplex-phase microstructure. *Acta Mater.* **2018**, *164*, 122–134. [[CrossRef](#)]
22. Kuzmina, M.; Ponge, D.; Raabe, D. Grain boundary segregation engineering and austenite reversion turn embrittlement into toughness: Example of a 9 wt.% medium Mn steel. *Acta Mater.* **2015**, *86*, 182–192. [[CrossRef](#)]
23. Hu, J.; Du, L.-X.; Xu, W.; Zhai, J.-H.; Dong, Y.; Liu, Y.-J.; Misra, R.D.K. Ensuring combination of strength, ductility and toughness in medium manganese steel through optimization of nano-scale metastable austenite. *Mater. Charact.* **2018**, *136*, 20. [[CrossRef](#)]
24. Li, Z.; Wu, D. Effects of Hot Deformation and Subsequent Austempering on the Mechanical Properties of Si-Mn TRIP Steels. *ISIJ Int.* **2006**, *46*, 121–128. [[CrossRef](#)]
25. GB/T 229; Metallic Materials-Charpy Pendulum Impact Test Method. Standards Press of China: Beijing, China, 2020.
26. Raabe, D.; Sandlöbes, S.; Millán, J.; Ponge, D.; Assadi, H.; Herbig, M.; Choi, P.-P. Segregation engineering enables nanoscale martensite to austenite phase transformation at grain boundaries: A pathway to ductile martensite. *Acta Mater.* **2013**, *61*, 6132–6152. [[CrossRef](#)]
27. Raabe, D.; Herbig, M.; Sandlöbes, S.; Li, Y.; Tytko, D.; Kuzmina, M.; Ponge, D.; Choi, P.-P. Grain boundary segregation engineering in metallic alloys: A pathway to the design of interfaces. *Curr. Opin. Solid State Mater. Sci.* **2014**, *18*, 253–261. [[CrossRef](#)]
28. Duchateau, D.; Guttman, M. Relationships between microstructure and mechanical properties of microduplex $\alpha + (\gamma + \epsilon)$ 6 and 9%Mn steels for cryogenic applications. *Met. Sci.* **1983**, *17*, 229–240. [[CrossRef](#)]
29. Zou, Y.; Xu, Y.; Wang, G.; Han, Y.; Teng, H.; Han, D.; Qiu, M.; Yang, F.; Misra, R. Improved strength-ductility-toughness balance of a precipitation-strengthened low-carbon medium-Mn steel by adopting intercritical annealing-tempering process. *Mater. Sci. Eng. A* **2020**, *802*, 140636. [[CrossRef](#)]
30. Ding, R.; Dai, Z.; Huang, M.; Yang, Z.; Zhang, C.; Chen, H. Effect of pre-existed austenite on austenite reversion and mechanical behavior of an Fe-0.2C-8Mn-2Al medium Mn steel. *Acta Mater.* **2018**, *147*, 59–69. [[CrossRef](#)]
31. Toji, Y.; Matsuda, H.; Herbig, M.; Choi, P.-P.; Raabe, D. Atomic-scale analysis of carbon partitioning between martensite and austenite by atom probe tomography and correlative transmission electron microscopy. *Acta Mater.* **2013**, *65*, 215–228. [[CrossRef](#)]

32. Matsuoka, Y.; Iwasaki, T.; Nakada, N.; Tsuchiyama, T.; Takaki, S. Effect of Grain Size on Thermal and Mechanical Stability of Austenite in Metastable Austenitic Stainless Steel. *ISIJ Int.* **2013**, *53*, 1224–1230. [[CrossRef](#)]
33. He, Y.; Li, L.; Luo, H.; Zhu, C. Ductile-brittle transition temperature of high-strength steel by Boltzmann function fitting method. *Phys. Exam. Test* **2020**, *38*, 7.
34. Gao, S.; Li, J.; Guo, L.; Bai, Q.; Li, F. Mechanical properties and low-temperature impact toughness of high-strength bolts after elevated temperatures. *J. Build. Eng.* **2022**, *57*, 104851. [[CrossRef](#)]
35. Jiang, J.; Wu, M.; Xu, T.; Bao, W.; Li, Z. Study on impact toughness of TMCP and quenched and tempered high strength steels. *Case Stud. Constr. Mater.* **2024**, *20*, e02795. [[CrossRef](#)]
36. Zeng, D.; An, T.; Zheng, S.; Dai, H.; Cao, Z.; Ma, C. Fracture toughness of weld metal of 440 MPa grade high-strength steel. *Chin. J. Mater. Trans.* **2024**, *38*, 151.

Disclaimer/Publisher’s Note: The statements, opinions and data contained in all publications are solely those of the individual author(s) and contributor(s) and not of MDPI and/or the editor(s). MDPI and/or the editor(s) disclaim responsibility for any injury to people or property resulting from any ideas, methods, instructions or products referred to in the content.